Applied Catalysis B: Environmental 301 (2022) 120781

Contents lists available at ScienceDirect

Applied Catalysis B: Environmental

journal homepage: www.elsevier.com/locate/apcatb

Copper-triggered delocalization of bismuth *p*-orbital favours high-throughput CO_2 electroreduction

Bowen Liu, Ying Xie, Xiaolei Wang, Chang Gao, Zhimin Chen *, Jun Wu, Huiyuan Meng, Zichen Song, Shichao Du, Zhiyu Ren *

Key Laboratory of Functional Inorganic Material Chemistry, Ministry of Education of the People's Republic of China, School of Chemistry and Materials Science, Heilongjiang University, 150080 Harbin, PR China

ARTICLE INFO

Keywords:
CO_2 reduction
Electrocatalyst
BiCu-bimetallic film
p-Orbital delocalization
High-throughput

ABSTRACT

At present, formic acid with the high energy value is the promising product generated by the large-scale renewable electricity-driven CO_2 conversion, yet challenges remain in the high-throughput and low-energy production accompanied by the considerable selectivity. Herein, in view of the contribution of electronic modulation to electrocatalytic CO_2 reduction reaction (CO_2RR) activity of catalysts, the thin BiCu-bimetallic film was designed and built on Cu foam (BiCu/CF) by coupling a facile hydrothermal reaction and an immediate electrochemical transformation. The theoretical evidences demonstrate that Bi *p*-orbital delocalization triggered by the close-contact metal Cu optimizes reaction pathway of CO_2RR, and also favours the orbital hybridization between Bi atom and *OCHO intermediate to form more anti-bonding orbitals, resulting in stabilizing *OCHO intermediate and lowering the thermodynamic barrier of CO_2RR. Meanwhile, the electron transferred from catalyst-sites to reaction species also accelerates during CO_2RR. Integrating the improved intrinsic activity of Bi catalytic-sites and the superiority of Cu foam in exposing more active sites and the mechanical strength, the BiCu/CF electrode with optimal thickness can acquire satisfactory indicators for industrial application, yielding a record formate current density of 856 mA cm^{-2}, higher than 85% Faradic efficiency, along with a remarkable stability, which outperforms state-of-the-art Bi-based catalysts. This study offers potential avenues of engineering orbital delocalization to rationally construct advanced CO_2RR electrodes for the carbon-neutral cycle and utilization.

1. Introduction

Electrochemical CO_2 conversion into the value-added chemical feedstocks driven by the renewable-powered electricity is a fascinating and promising strategy to mitigate the environmental and energy issues, achieving the carbon cycle, utilization, and neutralization [1–7]. Owing to the multiple electron/proton coupled transfer process, sixteen products with broad selectivity can be produced during the electrocatalytic CO_2 reduction reaction (CO_2RR) [8–11]. Although methane, methanol, ethanol and ethylene have the larger market sizes and higher market prices, formic acid (HCOOH) or formate ($HCOO^-$) shows an unparalleled advantage in the energy value (the price normalized to the chemical energy stored) due to their high energy efficiency and the specific selectivity [12–15]. Therefore, up till now, formic acid (or formate) is the most promising target product of large-scale production [16–18].

Over the last decades, metal catalysts (e.g. Sn, In, Bi, Pb, Pd, Hg, etc.), which have a weak affinity towards $CO_2^{\cdot-}$ and the partiality for forming the *OCHO intermediate, have been verified to motivate the selective conversion of CO_2 to HCOOH [8,19,20]. In particular, compared to other metals, Bi-based catalysts have drawn a broad attention as it can maximally meet the large-scale commercial needs in term of the cost-effectiveness [4], long-term stability [21], and environment-friendly nature [2,15,22]. Previous researches on Bi-based catalysts focused on further improving their electrocatalytic CO_2 performance by the structural engineering. For instance, Bi nanoparticles [23–25], Bi nanowires [26], Bi nanotubes [27,28], Bi dendrites [29–31], ultrathin Bi nanosheets [32], atomically thin bismuthene [33,34], and single atomic Bi [35,36] have been explored to catalyze CO_2 reduction. The common feature of these works is to maximize the utilization of Bi atoms in catalysts, resulting in the high energy conversion efficiency.

The electrocatalytic mechanism of CO_2RR was also extensively investigated deeply. The in-situ (or quasi-situ) experiments

* Corresponding authors.
E-mail addresses: zmchen@hlju.edu.cn (Z. Chen), zyren@hlju.edu.cn (Z. Ren).

https://doi.org/10.1016/j.apcatb.2021.120781
Received 21 June 2021; Received in revised form 7 September 2021; Accepted 27 September 2021
Available online 29 September 2021

demonstrated that metal Bi (and/or the low valence Bi) derived from the reduction process is the real catalytic sites for CO_2RR, because the applied potential of CO_2RR is usually lower than the standard potential of metal reduction [37–40]. Besides discriminating true active sites, exploring the powerful strategy to modulate the electronic structure of Bi-based catalysts is equally important, because it directly related to the intrinsic activity of catalysts. Recently, H. Peng *et al.* pointed out that the delocalization of Bi *p*-orbitals regulated by condensing the length of Bi-Bi bonds can facilitate CO_2RR via optimizing *OCHO adsorption [41]. It is worth noting that the study of modulating the localized Bi *p*-orbitals into delocalized states still remains in the infancy, because of lacking in an appropriate strategy. No doubt modulating the electronic structure of transition metal *d*-orbitals by *s/p*-state perturbing contribute effectively their electrocatalytic activity [42–44]. Conversely, we can deduce that Bi *p*-orbitals are also modulated by *d*-orbitals of transition metals due to the correlated interplay, which is in charge of the thermodynamic and dynamic barrier of CO_2RR, the orbital hybridization between Bi atom and key intermediates, and the electron transfer. Apparently, it's an opportunity for advancing CO_2RR activity of Bi-based catalysts.

In addition, most reported Bi-based catalysts either require more negative and narrow applied potentials (~ -0.8 V_{RHE}), or produce the low current densities under catalytic turnover condition [25]. As it is, these performance indicators are far from the industrial and economic viability that must integrate simultaneously the high throughput (current density > 300 mA cm^{-2}), the low cell voltage, the considerable Faradic efficiency (80–90% FE) and the excellent stability [4,45]. More recently, attention is gradually shifting to the construction of catalysts/electrodes for CO_2RR that can meet industrial needs [46–48]. However, the current results are more or less deficient in the above-mentioned performance index [16], and a great challenge remains in developing Bi-based CO_2RR electrodes suitable for industry [18]. The actual CO_2RR performances, strictly speaking, depend on the intrinsic features of electrode [49,50], including the intrinsic catalytic ability [51,52], the numbers of effective activity sites [53–55], the electrical conductivity [56], the selectivity [57,58], as well as the mechanical strength [59]. The self-supporting film electrode with metal foam as the current collector will be preferred by industry because of the superiority of metal foam in the excellent electrical conductivity, the large area to expose the active sites and the superior mechanical strength in long-term operation [56,57]. Recently, metal Bi has been deposited on the surface of Cu foam (CF) [30,60] and Cu foil [61,62] by electrochemical method. Unfortunately, CO_2RR performances of these electrodes are unsatisfactory, maybe due to lacking the close interaction between metal Bi and Cu substrate.

Inspired by above analysis, we investigate the effect of *p*-Orbital delocalization on CO_2 electroreduction using BiCu-bimetallic film as proof-of-concept studies. The BiCu pre-catalyst was first built on Cu foam (BiCu/CF-p) by a simple hydrothermal reaction, in which Cu^{2+} ions in-situ dissolved from CF and co-deposited with Bi^{3+} ions to form compact film. Such strategy not only facilitates the tight connection of the CuBi film layer to CF, but more importantly ensures the close interaction between Bi and Cu in CuBi film, which can reduce the ohmic resistance of the electrode itself and maximize the modulation effect of Cu on Bi. After the further electrochemical transformation, the derived BiCu-bimetal on CF (BiCu/CF) with an optimized thickness gives an unprecedentedly large formate current density ($J_{formate}$) of 856 mA cm^{-2} with FEs larger than 85% as well as the remarkable catalytic stability and reproducibility, which are very closer to the industrial demand. Both theoretical and experimental analyses demonstrate that the delocalized Bi *p*-orbitals motivated by metal Cu are in charge of adsorbing/stabilizing the *OCHO intermediate, lowering the thermodynamic barrier of the CO_2-to-HCOOH reaction, and accelerating the charge transfer.

2. Experimental section

2.1. Materials and chemicals

$Bi(NO_3)_3.5H_2O$, urea, and sucrose were purchased from Tianjin Kermel Chemical Reagent Co. Ltd. (China). All reagents were of analytical grade and were used as received from the suppliers without further purification. The water (DI water, 18.2 MΩ cm^{-1}) used throughout all experiments was purified through a Millipore system. CF was got from Hunan Corun New Energy Co. Ltd. (Changsha, China). The right size CF (e.g., 3 × 4 cm) was sonicated in acetone for 15 min to remove the oil contamination layer on the surface. After washed cleanly with water, the CF was sonicated in DI water for 15 min, subsequently was sonicated in 1 M HCl for 15 min to remove the oxide contamination layer on the surface, and washed with water and ethanol in sequence, and finally dried in vacuum.

2.2. Preparation of various BiCu/CF electrodes

2.2.1. Synthesis of BiCu/CF-p

BiCu thin layer grown on CF was prepared by a hydrothermal reaction. In a typical experiment, 0.3 mmol of urea and 0.1 mmol of sucrose were dispersed in 30 mL of DI water at room temperature (25 °C) to form a uniform solution, and then 0.1 mmol of $Bi(NO_3)_3.5$ H_2O was added under stirred for 10 min. Subsequently, the above mixed solution was transferred into a 50 mL Teflon-lined autoclave, and a piece of CF (3 ×4 cm) was immersed in the solution. Then, the Teflon-lined autoclave was sealed and then kept at 150 °C for 9 h. After the autoclave cooled down to room temperature, the obtained sample (labeled as BiCu/CF-0.1-p) was washed with water and ethanol several times in sequence, and then dried in the air. In addition, to illustrate the role of urea and sucrose, the samples named as BiCu/CF-0.1-p-s and BiCu/CF-0.1-p-u were respectively prepared by using the same hydrothermal procedure but only without adding urea or sucrose.

2.2.2. Synthesis of BiCu/CF

To obtain BiCu-bimetallic film on the surface of CF, a cathodic transformation was carried out by a simple chronoamperometry method using an electrochemical workstation (Princeton Applied Research, VersaSTAT 3F, USA) in a standard three-electrode system. Herein, the prepared BiCu/CF-0.1-p, Pt foil, and Ag/AgCl (saturated KCl-filled) electrode worked as the working electrode, auxiliary electrode, and reference electrode, respectively. Typically, a cathodic transformation is operated in 0.5 M $KHCO_3$ at the electrochemical reduction-potential of -1.0 V_{RHE} for 600 s. The obtained electrode is labelled as BiCu/CF-0.1.

As a control, the BiCu/CF with different thickness was also prepared by using the same procedure but only adjusting the amounts of $Bi(NO_3)_3$ added into the solution, such as 0.05, 0.075, 0.15, 0.2, and 0.25 mmol, and the obtained products were labeled as BiCu/CF-0.05, BiCu/CF-0.075, BiCu/CF-0.15, BiCu/CF-0.2, and BiCu/CF-0.25, respectively. In addition, commercial Bi powder (0.7 mg cm^{-2}) was also sprayed to the surface of CF to form a reference sample.

2.3. Characterizations

X-ray diffraction (XRD) was performed using a Bruker D8 ADVANCE diffractometer. Scanning electron microscopy (SEM, Hitachi S-4800) with an acceleration voltage of 15 kV and transmission electron microscopy (TEM, JEOL JEM-3010) with an acceleration voltage of 300 kV were used to observe and analyze the morphology of BiCu/CF. X-ray photoelectron spectroscopy (XPS) analysis was carried out using the Kratos Axis Ultra DLD. Inductively coupled plasma optical emission spectrometer (ICP-OES, Thermo Scientific iCAP 7600) was used to measure the contents of Cu and Bi in system. The gas and liquid products were quantitatively analyzed by the on-line gas chromatography (GC) equipped with TCD and FID detectors (Techcomp Scion 456 C) and ^1H

nuclear magnetic resonance spectroscopy (NMR, Bruker DRX 400 Avance MHz), respectively.

2.4. Electrochemical measurements

All electrochemical tests in H-cell and flow-cell were performed on Princeton electrochemical instrumentation equipment. As-prepared BiCu/CF was cut into 1.0 cm^{-2} as the working electrode. Pt foil and

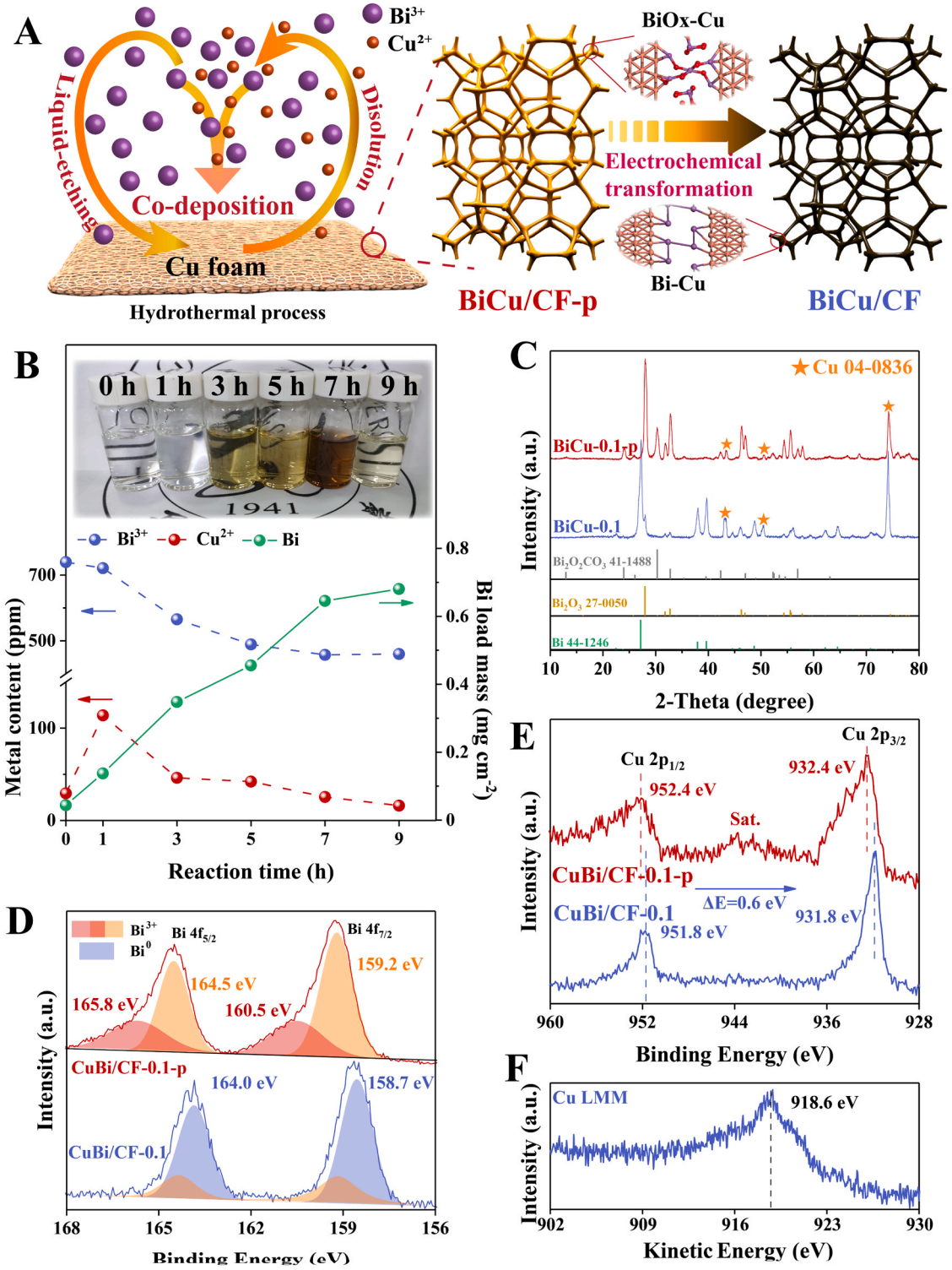

Fig. 1. Synthesis procedure and structure characterizations of BiCu/CF. (A) Schematic illustration of the synthesis procedure for BiCu/CF electrode. (B) The concentration change of Bi^{3+} and Cu^{2+} in the residual liquid and solid waste, and the content change of Bi loaded on CF along with the hydrothermal reaction time, analyzed by ICP-OES measurement. The insert in (B) is the optical photographs of the liquid supernatant at different reaction time. (C) XRD pattern of BiCu-0.1-p and BiCu-0.1 exfoliated from CF. (D-E) The high-resolution Bi *4f* and Cu *2p* XPS spectra of BiCu/CF-0.1-p and BiCu/CF-0.1, respectively. (F) Cu LMM Auger electron spectrum of BiCu/CF-0.1.

Ag/AgCl (saturated KCl-filled) or Hg/HgO (1 M KOH-filled) electrodes were used as the counter electrode and reference electrodes, respectively. All measured potentials were adjusted to a reversible hydrogen electrode (RHE) followed the equation: $E_{RHE} = E_{applied} + E_{reference} + 0.0592$ pH. The potential correction of the reference electrode was performed using the RHE electrode before each measurement was performed, in order to ensure correct test results. Linear sweep voltammetry (LSV) was recorded in CO_2/Ar-saturated 0.5 M $KHCO_3$ electrolyte at a scan of 1.0 mV s^{-1}. Chronopotentiometry was recorded via applying a constant current density on the working electrode. The electrochemical double-layer capacitance (C_{dl}) was calculated by a series of CV curves at various scan rates in the non-Faradaic region of 0 ~ 0.1 V_{RHE}. Electrochemical impedance spectra (EIS) were measured at an −0.2 ~ −0.6 V_{RHE} over a frequency range from 10^{-2} to 10^{5} Hz. The detailed operation processes are shown in the Electronic Supplementary Information (ESI). Meanwhile, the calculation methods about FEs of gas/liquid products and the power conversion efficiency (PCE) were also listed in ESI.

2.5. Computational details

All density function theory (DFT) calculations were performed by using the plane-wave technique implemented in the Vienna Ab Initio Simulation package (VASP). The detailed information displays in ESI.

3. Results and discussion

3.1. Synthesis and characterizations of BiCu/CF

The BiCu/CF electrode was prepared by coupling a facile hydrothermal reaction and an immediate electrochemical transformation, as illustrated in Fig. 1A. At the initial stage, Cu^{2+} ions are dissolved from the surface of CF due to the acid corrosion of $Bi(NO_3)_3$ solution (pH=3.24). During the hydrothermal process, Bi^{3+} and in-situ generated Cu^{2+} ions are then evolved into BiCu/CF-0.1-p, and meanwhile, the mass of Bi loaded on CF increases along with the hydrothermal reaction time (Fig. 1B). The X-ray diffraction (XRD) pattern of BiCu-0.1-p displays that Bi_2O_3 and $Bi_2O_2CO_3$ synchronously grown on the surface of CF (**Fig. 1** C). The slight XRD signals of Cu species, accompanied with the distinct reduction in Cu^{2+} content in the residual liquid and solid waste which is measured by inductively coupled plasma optical emission spectrometer (ICP-OES), suggest that Cu have been deposited on CF indeed (Fig. 1B and Table S1). More importantly, the maximum Cu^{2+} concentration in hydrothermal system reaching at 1 h of hydrothermal reaction demonstrates that the generated film can well inhibit the further dissolution of CF. The formation of BiCu-0.1-p mainly depends on the combination of urea and sucrose. The self-decomposition of urea makes the pH value of reaction system increase (Table S1), which in turn restrains the excessive corrosion of CF and contributes to the co-deposition of Cu^{2+} and Bi^{3+} ions (Fig. S1). While, sucrose in this system can assist BiCu film in growing on CF. As shown in Fig. S2, the XRD pattern of BiCu/CF-0.1-p-u prepared by using the same procedure but only without adding sucrose is more like that of pure CF. Meanwhile, the change in ionic charge and pH value gradually causes the flocculation and precipitation of caramel which is derived from the sucrose during the hydrothermal reaction [63,64]. Therefore, the color of liquid supernatant gradually changes from colorless to brown, then to light yellow (inset of Fig. 1B). After the electrochemical transformation (applying a constant potential of −1.0 V_{RHE} for 600 s), besides the weak BiO_x peaks perhaps induced by the spontaneous oxidation in air or derived metastable Bi oxides, the clear diffraction peaks assigned to metal Bi and Cu simultaneously appear in the XRD pattern of BiCu/CF-0.1 (Fig. 1C). Furthermore, we can prepare BiCu/carbon paper using the same procedure but only replacing CF with Cu^{2+} ions as the metal source (Fig. S3), which indirectly certifies the successful formation of BiCu film on CF.

Further XPS measurement was carried out to verify the component evolution of BiCu/CF-0.1 electrode. As shown in Fig. S4, Cu and Bi appear on the survey XPS spectra of BiCu/CF-0.1-p and BiCu/CF-0.1, and the Bi/Cu atom ratio is about 2:3 without change during the electrochemical transformation. It illustrates that metal Bi and Cu is present throughout the BiCu-bimetallic film. Bi *4f* XPS of BiCu/CF-0.1-p can be mainly deconvoluted into the couple peaks (164.5 and 159.2 eV ascribed to Bi_2O_3; 165.8 and 160.5 eV ascribed to $Bi_2O_2CO_3$) [65,66]. In contrast, a significant shift to the low binding energy occurs in the Bi *4f* XPS of BiCu/CF-0.1 [67], and the distinct Bi peaks located at 164.0 and 158.7 eV appear. Meanwhile, the slight XPS peaks assigned to Bi_2O_3 can also be observed, maybe due to the re-oxidation in air or produced metastable Bi oxides. These results tally with XRD analysis, confirming the conversion from Bi_2O_3 and $Bi_2O_2CO_3$ into metal Bi during the electrochemical reduction (Fig. 1D). However, the binding energy of Bi *4* $f_{7/2}$ located at 158.7 eV is higher than that of metal Bi (~157.0 eV) [39,68], which can possibly be attributed to the electron-transfer from Bi to Cu or surface oxidation. Bi species with lower oxide state generally serve as highly active catalytic-sits of CO_2-to-HCOOH conversion [23]. Meanwhile, comparing with Cu *2p* XPS spectrum of BiCu/CF-0.1-p (Cu $2p_{1/2}$ at 952.4 eV and Cu $2p_{3/2}$ at 932.4 eV), only clear peaks of metal Cu can be observed in Cu *2p* XPS of BiCu/CF-0.1, which is evidenced by the corresponding Auger electron spectrum (Cu LMM) (Fig. 1E and F). It manifests that CuO_x in BiCu film is reduced synchronously during the electrochemical transformation (Fig. 1E).

The morphology of BiCu/CF-0.1 was also characterized by scanning electron microscopy (SEM). The compact BiCu-bimetallic film uniformly covers the whole copper foam frame (Fig. 2A and S5). For BiCu/CF-0.1, the thickness of BiCu film on the surface of CF is about 109 nm as validated by the cross-sectional SEM image (Fig. 2B). Moreover, the thickness of BiCu-bimetallic film can be adjusted to 232 nm by increasing the Bi load mass (normalized to the geometric area of CF) (Fig. 2B and S6). There is no doubt that excessive Bi deposited into the BiCu-bimetallic film reduces the probability of close contact between Bi and Cu. Unfortunately, once the amount of $Bi(NO_3)_3.5H_2O$ added into the solution reduces, plenty of defects like cavities and rifts emerge on CF (Fig. S7), and therefore a thinner BiCu-bimetallic film less than 109 nm cannot be constructed on the surface of CF. The BiCu-bimetallic film exfoliated from CF presents sheet-like structure (Fig. 2C and D). From the high-resolution TEM images (Fig. 2E and F), the distinct lattice fringes corresponding to (012) (d_{012} = 0.33 nm) plane of metal Bi and (111) (d_{111} = 0.21 nm) plane of metal Cu are most frequently observed in BiCu-bimetallic film, which illustrates metal Bi intermingles with metal Cu closely. Evidences from the scanning TEM-energy-dispersive X-ray spectroscopy (STEM-EDS) mapping (Fig. 2G) further verifies the uniform distribution of Bi on the surface of CF. Such close contact maximizes the regulating effect of Cu on the electronic structure of Bi catalytic-site, thus promoting the catalytic ability of BiCu/CF-0.1 electrode towards CO_2RR.

3.2. Electrocatalytic CO_2RR activity and mechanism of BiCu/CF electrode

The CO_2RR activity of BiCu/CF-0.1 electrode was first assessed in a gas-tight H-cell (see details in the Experimental section). The linear sweep voltammetry curves (LSVs) show that BiCu/CF-0.1 electrode is aroused at −0.6 V_{RHE} in CO_2-saturated 0.5 M $KHCO_3$ electrolyte, derived from the response to CO_2RR (Fig. 3A). After that, a sharp increase in its current densities is accompanied by applying more negative potentials, indicating the high sensitivity of BiCu/CF-0.1 electrode towards CO_2RR relative to the hydrogen evolution reaction (HER). The detailed evaluation towards CO_2RR at each applied potential was displayed in the chronoamperometric response (Fig. S8), and the corresponding Faradaic efficiencies (FEs) of gas and liquid products were quantified by the on-line GC and the off-line ^{1}H NMR analysis. Clearly, HCOOH, CO and H_2 are produced simultaneously during the electrocatalytic CO_2 process (Fig. 3B). Relative to the CO_2-to-CO conversion

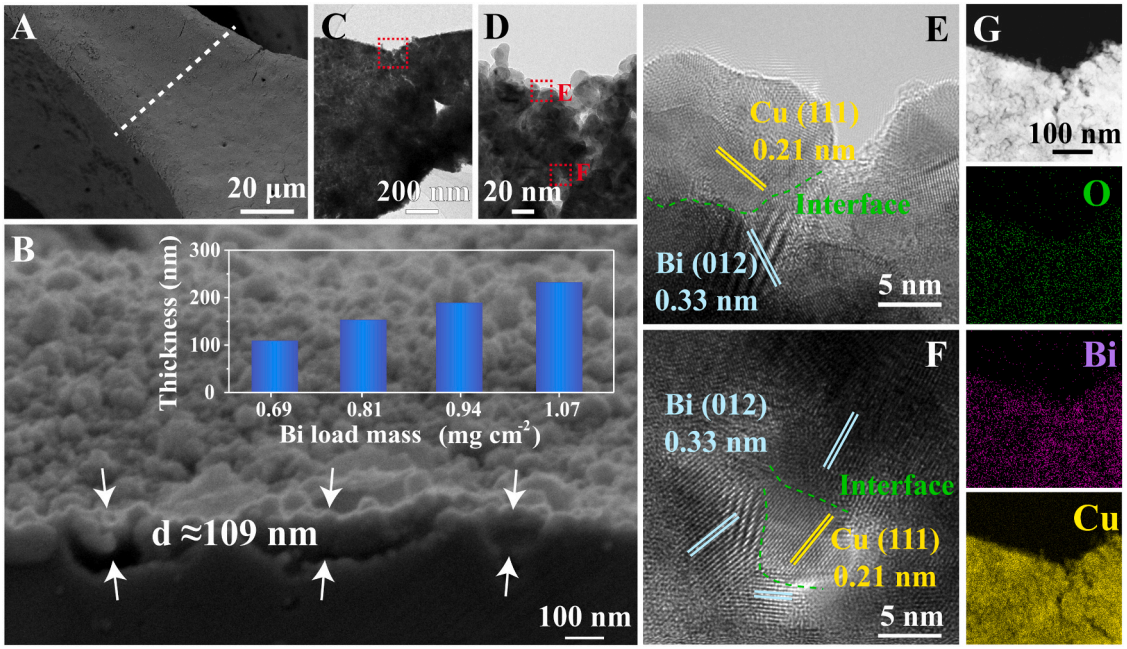

Fig. 2. Microscopic morphology of BiCu/CF-0.1. (A, B) Typical top-view and cross-sectional SEM images of BiCu/CF-0.1. The insert in (B) is the relationships between layer thickness and Bi load mass on CF. (C-G) TEM images, high-resolution TEM images and STEM-EDS mapping of BiCu exfoliated from CF.

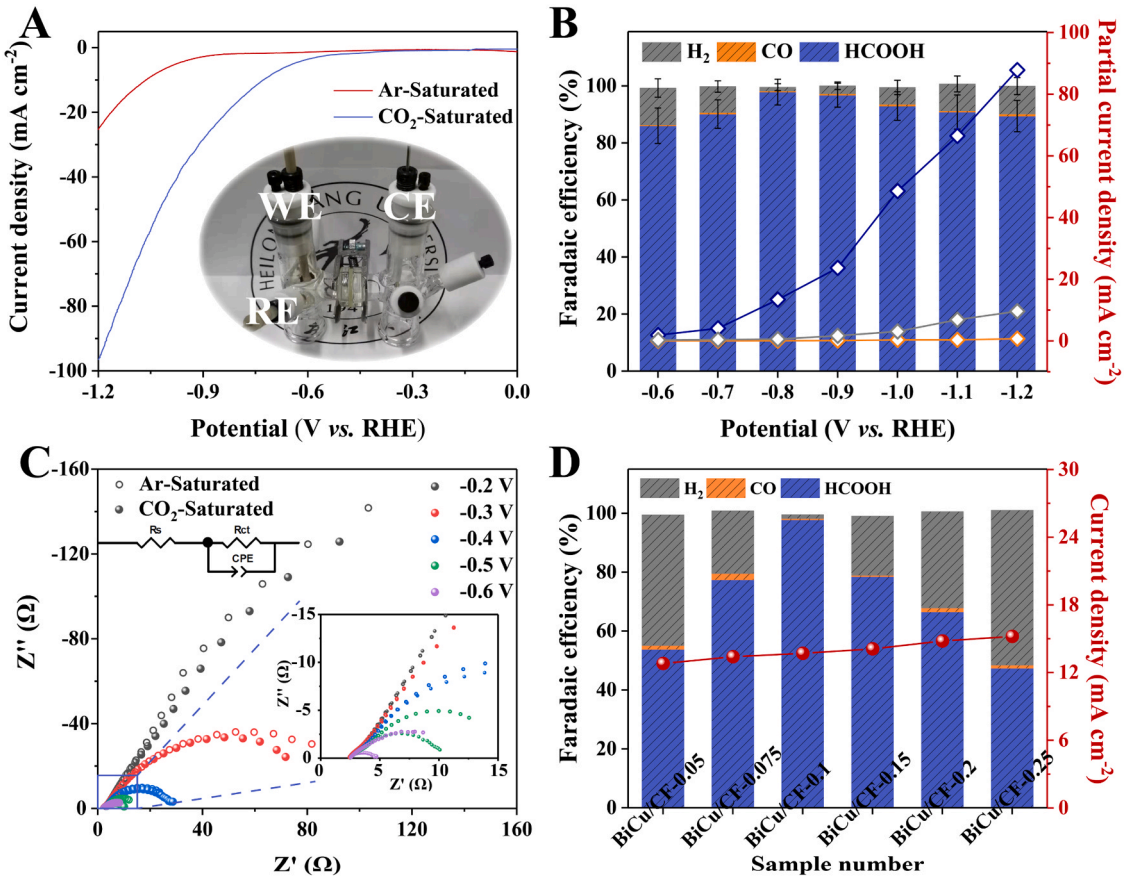

Fig. 3. Electrochemical CO_2RR performance of BiCu/CF electrode in an H-cell. (A) LSVs of CO_2RR measured in CO_2/Ar-saturated 0.5 M $KHCO_3$ solution (scan rate: 1 mV s^{-1}). The insert in (A) is the optical photograph of the H-typical cell. (B) Reduction potential-dependent FEs and partial current densities of HCOOH, CO, and H_2 for BiCu/CF-0.1. (C) Comparison of potential-dependent Nyquist plots for BiCu/CF-0.1 measured in CO_2/Ar-saturated 0.5 M $KHCO_3$ aqueous solution. The inserts in (C) are the enlarged view and the equivalent circuit diagram (R_s: the electrolyte resistance; R_{ct}: the charge-transfer resistance), respectively. (D) FEs and current densities at −0.8 V_{RHE} of various BiCu/CF electrodes.

and HER, BiCu/CF-0.1 has a significant advantage in selectively catalyzing CO_2 into HCOOH. All FEs of HCOOH are over 85% in a wide range of applied potentials (from −0.6 to −1.2 V_{RHE}), much higher than that of CO and H_2. The maximum average FE of HCOOH can achieve 94.2% when the applied potential is −0.8 V_{RHE}. The difference is that bare CF tends to produce hydrogen, more than 95% FEs of H_2 in the whole applied potential (Fig. S9). The partial current densities of all products calculated based on the total current densities and the corresponding FEs further compare the capability of selective catalyzing CO_2. Keep with the LSVs, the partial current densities, especially $J_{formate}$, dramatically increase sequentially in the applied potential; whereas, the partial current density of H_2 and CO only shows a slight increase. Sure enough, the bare CF gives the opposite change-trend in partial current density (Fig. S9). All above results demonstrate that BiCu-bimetallic film drives the formation of HCOOH. Noticeably, as shown in Fig. S10 and Table S2, $J_{formate}$ of BiCu/CF-0.1 overall applied potentials from −0.6 to −1.2 V_{RHE} were always much larger than those of recently reported Bi-based electrocatalysts, which is a crucial competitive advantage for achieving large current density in industrial utilization of CO_2RR electrocatalysts.

Further, the charge-transfer resistance (R_{ct}) of BiCu/CF-0.1 and CF at various applied potentials are compared by fitting the corresponding electrochemical impedance spectra (EIS). The R_{ct} values of BiCu/CF-0.1 and CF continuously reduce as the applied potentials change from −0.2 V_{RHE} to −0.6 V_{RHE} (Fig. 3C, S11, and Table S3). It is noteworthy that, at the onset potential of CO_2RR (−0.6 V_{RHE}), the R_{ct} value of BiCu/CF-0.1 in CO_2-saturated $KHCO_3$ solution decreases remarkably compared to the almost constant R_{ct} value in Ar-saturated $KHCO_3$ solution. It demonstrates that BiCu/CF-0.1 prefers to rapidly transfer electrons to CO_2 and intermediates, resulting in an accelerated kinetic

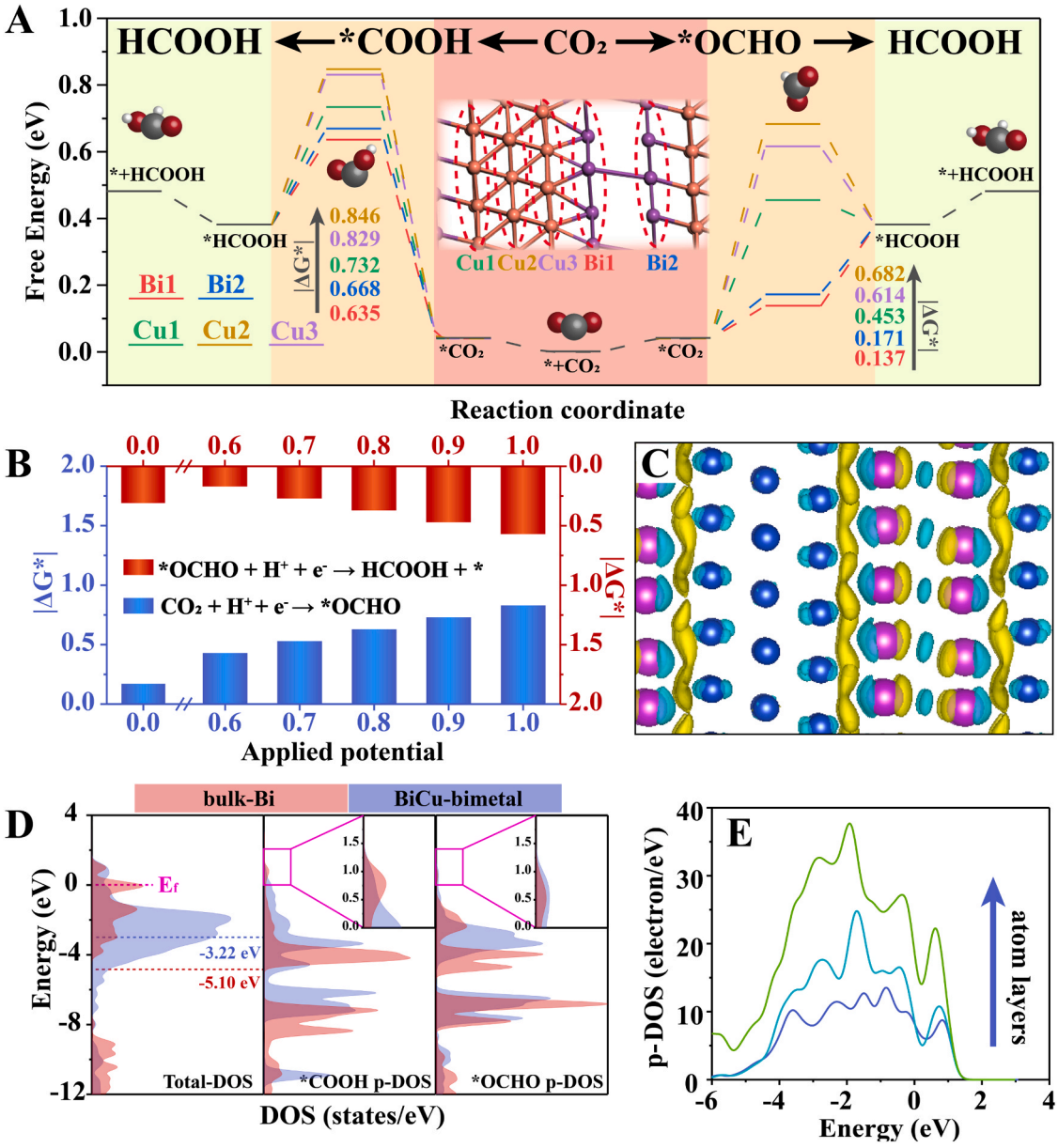

Fig. 4. Electrocatalytic CO_2RR mechanism of BiCu/CF electrode. (A) Calculated free energies for CO_2RR on five sites of Cu-Bi model (U_{RHE} = 0 V). The inset is the optimized Cu-Bi model. (B) The corresponding |ΔG* | values of the interface Bi2 site for CO_2RR at different applied potentials. (C) Charge density distribution of Cu-Bi model (yellow: charge accumulation, blue: charge depletion). (D) Calculated bulk-Bi DOS (pink), BiCu-bimetal DOS (blue), and p-DOS of *OCHO and *COOH adsorbed on metal Bi and BiCu bimetal, respectoively. (E) Calculated projected DOS of Bi *p*-orbitals (navy-blue line: two Bi-atom layers, light-blue line: three Bi-atom layers, and yellow-green line: four Bi-atom layers).

process. Furthermore, the R_{ct} value of CF at each potential is larger than that of BiCu/CF-0.1, implying that bare CF is insensitive to CO_2RR.

In addition, the influence of Bi amount on catalytic CO_2RR performance was also investigated. For CO_2RR, with increasing Bi amount in BiCu-bimetallic film, the HCOOH FE first displays a dramatic increase from 53.8% to 97.8%, and then drops to 47.4% (Fig. 3D and Fig. S12). The best CO_2RR performance is achieved when the film thickness is 109 nm. The electrochemical double-layer capacitance (C_{dl}) of various BiCu/CF electrodes clarify that the more Bi species, the larger electrochemically active surface areas (Fig. S13). At the high Bi amount, the decrease in CO_2RR performance is likely to attribute to the gradually weakened electron-modulating capacity of the underlying Cu (including CF and re-deposited metal Cu) for the superficial Bi metal, which reduces the intrinsic catalytic ability of catalytic sites. Further evidences from the potential-dependent FEs of commercial Bi powder on CF support it (Fig. S14).

Systematic density functional theory (DFT) calculations were performed to explore the catalytic mechanism of BiCu/CF towards CO_2RR. To simplify the calculation system, only the model of metallic Bi-Cu heterogeneous interface was constructed based on the experimental analysis to simulate BiCu-bimetallic film. Five sites adjacent to the Cu-Bi interface were selected to adsorb the intermediates (the inset in Fig. 4A and S15). Two various reaction pathways of the CO_2-to-HCOOH conversion on BiCu bimetal, bulk Bi and bulk Cu are compared in Fig. 4A and S16. It is apparent that BiCu bimetal is more energetic for CO_2RR relative to bulk Bi and Cu (Table S3). Owing to the lower thermodynamic barrier, CO_2 prefers to form *OCHO intermediate on the five sites, instead of the *COOH intermediate to produce HCOO or CO (Fig. 4A, S17A and Table S4). Moreover, in contrast to the competitive hydrogen evolution reaction, CO_2RR occurs more readily on the BiCu/CF electrode, which fits exactly with the electrochemical tests (Fig. 4A and S17B). In *OCOH pathway, Bi sites at the Cu-Bi interface show the durative uphill thermodynamic barriers for CO_2RR, and the rate-determining step (RDS) in kinetics is the second elementary process ($*OCHO + e^- + H^+ \rightarrow *HCOOH$), not the previous process ($* + CO_2 + e^- + H^+ \rightarrow *OCHO$), which is opposite to CO_2RR on bulk Bi. It well coincides with the Tafel slope of BiCu/CF (51.7 mV dec^{-1}), close to the theoretical value (59 mV dec^{-1}) for a rapid protonation of CO_2 followed by HCOOH-RDS step (Fig. S18) [9,69]. Moreover, relative to other sites indicated in Fig. 4A, the $|\Delta G^*|$ value of RDS on the interface Bi2 site is small, illustrating that Bi2 site is the preferential catalytic-site for HCOOH formation (Fig. 4A and Table S3). Further evidences from the reaction free energies of the interface Bi2 site at different applied potentials verify that the applied potential reduces the thermodynamic barrier of CO_2 protonation, the more negative potential, the lower barrier (Fig. 4B, S19, and Table S5), which greatly stimulates CO_2RR. These results tally with the increase of reaction rate and HCOOH partial current density at negative potential indicated in the electrochemical testing (Fig. 3B and C).

As evidences from the calculated charge density distribution of BiCu-bimetal (Fig. 4C), at the Bi-Cu interface, the electrons of Bi atoms be partial to Cu atoms closely connected to them and therefore Bi atoms are electropositive, which matches XPS analysis well. Similarly, compared to bulk Bi, the distinct delocalization of Bi *p*-orbitals emerges in the calculated projected density of electronic states (DOS) (Fig. S20) [41, 43]. The strong delocalization of Bi electrons favors the orbital hybridization between the catalytic site and *OCHO (or *COOH) intermediate to form more anti-bonding orbitals, clearly optimizing the interaction energies of CO_2RR (Fig. 4D) [42,44]. As the solid evidences, in comparison to bulk Bi, the total DOS center of BiCu-bimetal is closer to the Fermi level and the p-orbital DOS of *OCHO and *COOH adsorbed on the catalyst have most of the cleavage at the Fermi level, signifying the enhanced interactions with *OCHO and *COOH intermediates [14, 70–73]. Note that the trend of electron transfer and Bi *p*-orbital delocalization gradually declines as the Bi-atom layers covered on interfacial Cu increase (Fig. 4E). When the distance gradually increases, namely Bi content increasing, the charge density of Bi atoms is identical to that of bulk Bi (Fig. S21A), and the centers of *p*-orbital DOS and total DOS also move away from the Fermi energy level again (Fig. S21B). Only the interfacial Bi atoms have a high bond strength with *OCHO and *COOH intermediate as evidenced by the more cleavage at the Fermi level; whereas, the Bi atoms far away from the Cu-Bi interface is like metal Bi (Fig. S21C, D). That's why BiCu-bimetallic film with thin thickness maximumly stimulates CO_2RR. It follows that the *p*-orbitals delocalization of Bi is responsible for the energetic CO_2RR on BiCu/CF in terms of lowing the thermodynamic barrier of CO_2RR, stabilizing *OCHO intermediate, and accelerating the electron transfer from catalytic-site to reaction species.

3.3. High-throughput CO_2-to-HCOOH conversion on BiCu/CF-0.1 electrode

To highlight the superiority of BiCu/CF-0.1 in the high-throughput CO_2-to-HCOOH conversion, the CO_2RR performance of BiCu/CF-0.1 was studied using a customized flow-cell and an alkaline electrolyte (Fig. 5A). As depicted in Fig. 5B, with the full supply of CO_2, high current densities from 100 to 1000 mA cm^{-2} can be achieved on BiCu/CF-0.1 electrode in the applied potential range from − 0.63 to − 2.41 V_{RHE}. It is rather remarkable that the high current density is not at the expense of FE, a 92.1% FE of HCOOH at 300 mA cm^{-2}. Even at a record current density of 1000 mA cm^{-2} ($J_{formate}$ of 856 mA cm^{-2}), the FE of HCOOH is above 85%. Meanwhile, at various current densities, BiCu/CF-0.1 displays good durability with no evident loss in terms of applied potential and FEs, even at 100–1000 mA cm^{-2} for 80 h (Fig. 5C and S22). Furthermore, the long-term storage stability and cycling reproducibility of BiCu/CF-0.1 was also assessed by measuring CO_2RR at intervals of 6 days. Although BiCu/CF-0.1 is spontaneously oxidized again to form BiO_x layer on its surface after long-term storage in air (Fig. S23), evidences from Fig. S24 show that BiCu/CF-0.1 is also sensitive to the selective conversion from CO_2 into HCOOH after being re-activated by the prior electrochemical transformation. The superior stability and reproducibility of BiCu/CF-0.1 in catalyzing CO_2RR during redox cycle can be attributed to its stable structure reversibility and good mechanical strength. In comparison with other reported state-of-the-art Bi-based catalysts, BiCu/CF-0.1 showed an extremely high current density with satisfactory FE for CO_2-to-HCOOH (Fig. 5D, and Table S6).

In view of the above gratifying results, a two-electrode electrolyzer was assembled with BiCu/CF-0.1 and Pt foil as cathodic CO_2RR and anodic oxygen evolution catalyst to assess its catalytic capacity in the practical implementation (designed as BiCu/CF-0.1||Pt foil). Driven by the cell voltage, cathodic CO_2RR occurs on BiCu/CF-0.1 and the peak of HCOOH FEs reaches 93.4% at 3.2 V (Fig. S25). During a 10 h CO_2RR operation, a nearly constant HCOOH selectivity (90.2% FE of HCOOH) and a cathodic power conversion efficiency of 35% can be achieved at 100 mA cm^{-2}, well revealing the potential of BiCu/CF-0.1 in practical applications.

4. Conclusions

In summary, this work interprets the contribution of *p*-orbital delocalization in enhanced CO_2RR performances of BiCu/CF in detail. Experimental and DFT results have revealed that the resultant BiCu/CF capable of motivating the orbital hybridization of Bi-*OCHO, stabilizing *OCHO intermediate, and lowering the thermodynamic barrier of CO_2RR, which is related to Bi *p*-orbital delocalization triggered by metal Cu. Benefiting from the features in its mechanical strength and structure, BiCu/CF electrode elevated HCOOH production up to 85.6% FE with a current density of 1000 mA cm^{-2} in flow-cell testing. The fundamental exploration exuded by this study is indicative to design the superior electrode in future researches.

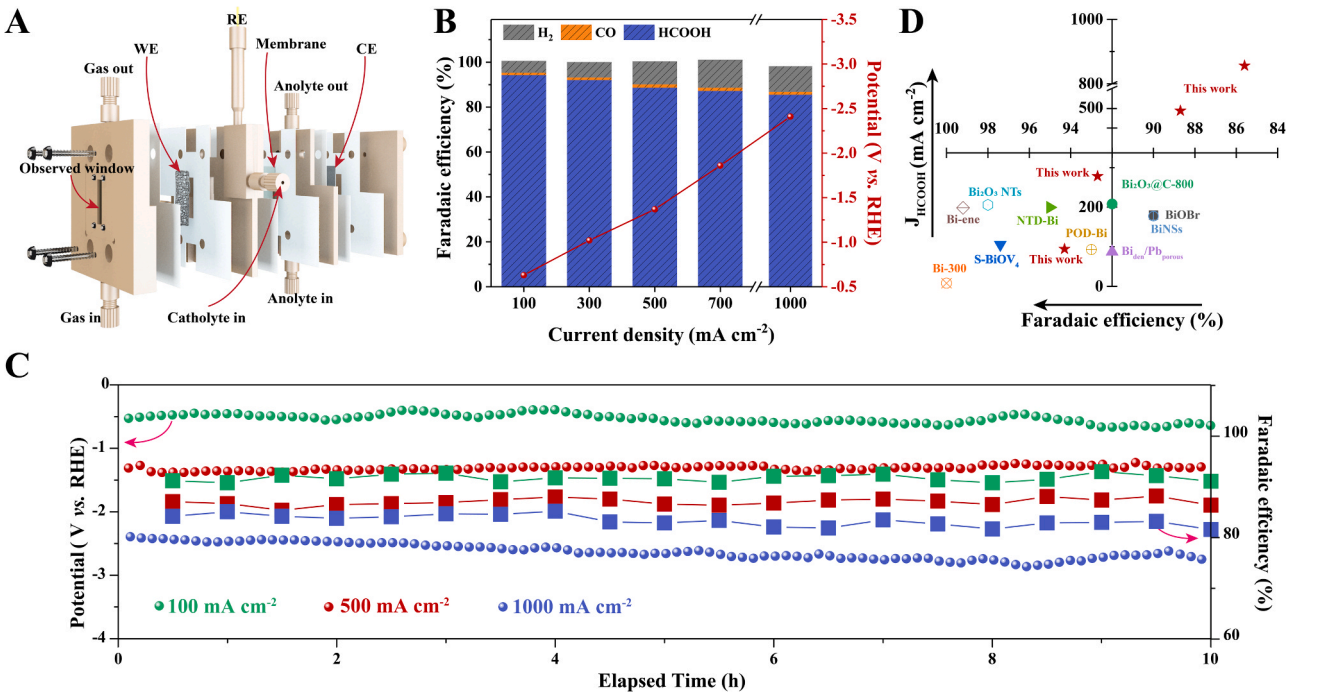

Fig. 5. Electrochemical CO_2RR performance of BiCu/CF-0.1 electrode in a flow-cell. (A) Schematic diagram of flow-cell. (B) Reduction current-dependent FEs of HCOOH, CO, and H_2 and the corresponding potentials. (C) The potential response and the corresponding FEs of BiCu/CF-0.1 at different current densities as indicated. All results are measured in 1.0 M KOH solution. (D) The FEs and current density of BiCu/CF-0.1 in comparison with reported Bi-based electrocatalyst (flow-cell).

Supporting Information

Electronic Supplementary Information (ESI) available: Experimental section, computational details, and additional figures and tables regarding XRD and XPS analysis, SEM images, electrochemical measurements, DFT calculations and CO_2RR performance comparison.

CRediT authorship contribution statement

Bowen Liu: Catalyst preparation, Data collection and processing, Writing – original draft preparation. **Ying Xie:** Density functional theory calculations and Discussion. **Xiaolei Wang:** Results analysis and Discussion. **Chang Gao:** Experiment investigation. **Zhimin Chen:** Methodology, Ideas, Writing – review & editing. **Jun Wu:** Characterizations and Discussion. **Huiyuan Meng:** Electrochemical measurements; **Zichen Song:** Data analysis and Figure preparation. **Shichao Du:** Validation and Analysis. **Zhiyu Ren:** Supervision, Conceptualization, Writing – review & editing.

Declaration of Competing Interest

The authors declare that they have no known competing financial interests or personal relationships that could have appeared to influence the work reported in this paper.

Acknowledgment

We gratefully acknowledge the support by the National Key R&D Program of China (2018YFE0201704), the National Natural Science Foundation of China (22179035, 21631004 and 21901065), the Natural Science Foundation of Heilongjiang Province of China (LH2020B019), and the University Nursing Program for Young Scholars with Creative Talents in Heilongjiang Province (UNPYSCT-2018009).

Appendix A. Supporting information

Supplementary data associated with this article can be found in the online version at doi:10.1016/j.apcatb.2021.120781.

References

[1] Y. Wang, P. Han, X. Lv, L. Zhang, G. Zheng, Defect and interface engineering for aqueous electrocatalytic CO_2 reduction, Joule 2 (2018) 2551–2582.
[2] Q. Wang, Y. Lei, D. Wang, Y. Li, Defect engineering in earth-abundant electrocatalysts for CO_2 and N_2 reduction, Energy Environ. Sci. 12 (2019) 1730–1750.
[3] J.B. Greenblatt, D.J. Miller, J.W. Ager, F.A. Houle, I.D. Sharp, The technical and energetic challenges of separating (Photo)electrochemical carbon dioxide reduction products, Joule 2 (2018) 381–420.
[4] M.G. Kibria, J.P. Edwards, C.M. Gabardo, C.T. Dinh, A. Seifitokaldani, D. Sinton, E. H. Sargent, Electrochemical CO_2 reduction into chemical feedstocks: from mechanistic electrocatalysis models to system design, Adv. Mater. 31 (2019), 1807166.
[5] R. Zhao, P. Ding, P. Wei, L. Zhang, Q. Liu, Y. Luo, T. Li, S. Lu, X. Shi, S. Gao, A. M. Asiri, Z. Wang, X. Sun, Recent progress in electrocatalytic methanation of CO_2 at ambient conditions, Adv. Funct. Mater. 31 (2021).
[6] X. Gao, B. Guo, C. Guo, Q. Meng, J. Liang, J. Liu, Zirconium-based metal-organic framework for efficient photocatalytic reduction of CO_2 to CO: the influence of doped metal ions, ACS Appl. Mater. Interfaces 12 (2020) 24059–24065.
[7] D.-D. Ma, S.-G. Han, C. Cao, W. Wei, X. Li, B. Chen, X.-T. Wu, Q.-L. Zhu, Bifunctional single-molecular heterojunction enables completely selective CO_2-to-CO conversion integrated with oxidative 3D nano-polymerization, Energy Environ. Sci. 14 (2021) 1544–1552.
[8] A. Vasileff, C. Xu, Y. Jiao, Y. Zheng, S.-Z. Qiao, Surface and interface engineering in copper-based bimetallic materials for selective CO_2 electroreduction, Chem 4 (2018) 1809–1831.
[9] Z. Sun, T. Ma, H. Tao, Q. Fan, B. Han, Fundamentals and challenges of electrochemical CO_2 reduction using two-dimensional materials, Chem 3 (2017) 560–587.
[10] Z. Chen, G. Zhang, L. Du, Y. Zheng, L. Sun, S. Sun, Nanostructured cobalt-based electrocatalysts for CO_2 reduction: recent progress, challenges, and perspectives, Small 16 (2020), 2004158.
[11] X. Li, Q.-L. Zhu, MOF-based materials for photo- and electrocatalytic CO_2 reduction, EnergyChem 2 (2020), 100033.
[12] Q. Hao, C. Liu, G. Jia, Y. Wang, H. Arandiyan, W. Wei, B.-J. Ni, Catalytic reduction of nitrogen to produce ammonia by bismuth-based catalysts: state of the art and future prospects, Mater. Horiz. 7 (2020) 1014–1029.

[13] C. Xia, P. Zhu, Q. Jiang, Y. Pan, W. Liang, E. Stavitsk, H.N. Alshareef, H. Wang, Continuous production of pure liquid fuel solutions via electrocatalytic CO_2 reduction using solid-electrolyte devices, Nat. Energy 4 (2019) 776–785.

[14] X. Zhang, Y. Zhang, Q. Li, X. Zhou, Q. Li, J. Yi, Y. Liu, J. Zhang, Highly efficient and durable aqueous electrocatalytic reduction of CO_2 to HCOOH with a novel bismuth–MOF: experimental and DFT studies, J. Mater. Chem. A 8 (2020) 9776–9787.

[15] S.-F. Leung, H.-C. Fu, M. Zhang, A.H. Hassan, T. Jiang, K.N. Salama, Z.L. Wang, J.-H. He, Blue energy fuels: converting ocean wave energy to carbon-based liquid fuels via CO_2 reduction, Energy Environ. Sci. 13 (2020) 1300–1308.

[16] N. Han, P. Ding, L. He, Y. Li, Y. Li, Promises of main group metal–based nanostructured materials for electrochemical CO_2 reduction to formate, Adv. Energy Mater. 10 (2019), 1902338.

[17] W. Zhang, Y. Hu, L. Ma, G. Zhu, Y. Wang, X. Xue, R. Chen, S. Yang, Z. Jin, Progress and perspective of electrocatalytic CO_2 reduction for renewable carbonaceous fuels and chemicals, Adv. Sci. 5 (2018), 1700275.

[18] Y. Song, X. Zhang, K. Xie, G. Wang, X. Bao, High-temperature CO_2 electrolysis in solid oxide electrolysis cells: developments, challenges, and prospects, Adv. Mater. 31 (2019), 1902033.

[19] F. Li, D.R. MacFarlane, J. Zhang, Recent advances in the nanoengineering of electrocatalysts for CO_2 reduction, Nanoscale 10 (2018) 6235–6260.

[20] K. Saravanan, Y. Basdogan, J. Dean, J.A. Keith, Computational investigation of CO_2 electroreduction on tin oxide and predictions of Ti, V, Nb and Zr dopants for improved catalysis, J. Mater. Chem. A 5 (2017) 11756–11763.

[21] L. Yi, J. Chen, P. Shao, J. Huang, X. Peng, J. Li, G. Wang, C. Zhang, Z. Wen, Molten salt assisted synthesis of bismuth nanosheets for long-term continuously electrocatalytic conversion CO_2 to formate, Angew. Chem. Int. Ed. 132 (2020) 20287–20294.

[22] J. Albo, M. Alvarez-Guerra, P. Castaño, A. Irabien, Towards the electrochemical conversion of carbon dioxide into methanol, Green Chem. 17 (2015) 2304–2324.

[23] P. Deng, H. Wang, R. Qi, J. Zhu, S. Chen, F. Yang, L. Zhou, K. Qi, H. Liu, B.Y. Xia, Bismuth oxides with enhanced bismuth–oxygen structure for efficient electrochemical reduction of carbon dioxide to formate, ACS Catal. 10 (2019) 743–750.

[24] Z. Zhang, M. Chi, G.M. Veith, P. Zhang, D.A. Lutterman, J. Rosenthal, S. H. Overbury, S. Dai, H. Zhu, Rational design of Bi nanoparticles for efficient electrochemical CO_2 reduction: the elucidation of size and surface condition effects, ACS Catal. 6 (2016) 6255–6264.

[25] M.Y. Zu, L. Zhang, C. Wang, L.R. Zheng, H.G. Yang, Copper-modulated bismuth nanocrystals alter the formate formation pathway to achieve highly selective CO_2 electroreduction, J. Mater. Chem. A 6 (2018) 16804–16809.

[26] M. Fan, S. Prabhudev, S. Garbarino, J. Qiao, G.A. Botton, D.A. Harrington, A. C. Tavares, D. Guay, Uncovering the nature of electroactive sites in nano architectured dendritic Bi for highly efficient CO_2 electroreduction to formate, Appl. Catal. B: Environ. 274 (2020), 119031.

[27] K. Fan, Y. Jia, Y. Ji, P. Kuang, B. Zhu, X. Liu, J. Yu, Curved surface boosts electrochemical CO_2 reduction to formate via bismuth nanotubes in a wide potential window, ACS Catal. 10 (2019) 358–364.

[28] P. Lu, D. Gao, H. He, Q. Wang, Z. Liu, S. Dipazir, M. Yuan, W. Zu, G. Zhang, Facile synthesis of a bismuth nanostructure with enhanced selectivity for electrochemical conversion of CO_2 to formate, Nanoscale 11 (2019) 7805–7812.

[29] J.H. Koh, D.H. Won, T. Eom, N.-K. Kim, K.D. Jung, H. Kim, Y.J. Hwang, B.K. Min, Facile CO_2 electro-reduction to formate via oxygen bidentate intermediate stabilized by high-index planes of bi dendrite catalyst, ACS Catal. 7 (2017) 5071–5077.

[30] X. Zhang, X. Sun, S.-X. Guo, A.M. Bond, J. Zhang, Formation of lattice-dislocated bismuth nanowires on copper foam for enhanced electrocatalytic CO_2 reduction at low overpotential, Energy Environ. Sci. 12 (2019) 1334–1340.

[31] Z.B. Hoffman, T.S. Gray, Y. Xu, Q. Lin, T.B. Gunnoe, G. Zangari, High selectivity towards formate production by electrochemical reduction of carbon dioxide at copper-bismuth dendrites, ChemSusChem 12 (2019) 231–239.

[32] F. Li, G.H. Gu, C. Choi, P. Kolla, S. Hong, T.-S. Wu, Y.-L. Soo, J. Masa, S. Mukerjee, Y. Jung, J. Qiu, Z. Sun, Highly stable two-dimensional bismuth metal-organic frameworks for efficient electrochemical reduction of CO_2, Appl. Catal. B: Environ. 277 (2020), 119241.

[33] Y. Zhang, X.L. Zhang, Y.Z. Ling, F.W. Li, A.M. Bond, J. Zhang, Controllable synthesis of few-layer bismuth subcarbonate by electrochemical exfoliation for enhanced CO_2 reduction performance, Angew. Chem. Int. Ed. 57 (2018) 13283–13287.

[34] S. Cao, B. Shen, T. Tong, J. Fu, J. Yu, 2D/2D heterojunction of ultrathin MXene/Bi_2WO_6 nanosheets for improved photocatalytic CO_2 reduction, Adv. Funct. Mater. 28 (2018), 1800136.

[35] Z. Chen, K. Mou, X. Wang, L. Liu, Nitrogen-doped graphene quantum dots enhance the activity of Bi_2O_3 nanosheets for electrochemical reduction of CO_2 in a wide negative potential region, Angew. Chem. Int. Ed. 57 (2018) 12790–12794.

[36] X. Yang, Y. Chen, L. Qin, X. Wu, Y. Wu, T. Yan, Z. Geng, J. Zeng, Boost selectivity of HCOO(-) using anchored Bi single atoms towards CO_2 reduction, ChemSusChem 13 (2020) 6307–6311.

[37] J. Medina-Ramos, S.S. Lee, T.T. Fister, A.A. Hubaud, R.L. Sacci, D.R. Mullins, J. L. DiMeglio, R.C. Pupillo, S.M. Velardo, D.A. Lutterman, J. Rosenthal, P. Fenter, Structural dynamics and evolution of bismuth electrodes during electrochemical reduction of CO_2 in imidazolium-based ionic liquid solutions, ACS Catal. 7 (2017) 7285–7295.

[38] J.E. Pander, M.F. Baruch, A.B. Bocarsly, Probing the mechanism of aqueous CO_2 reduction on post-transition-metal electrodes using ATR-IR spectroelectrochemistry, ACS Catal. 6 (2016) 7824–7833.

[39] C. Cao, D.D. Ma, J.F. Gu, X. Xie, G. Zeng, X. Li, S.G. Han, Q.L. Zhu, X.T. Wu, Q. Xu, Metal-organic layers leading to atomically thin bismuthene for efficient carbon dioxide electroreduction to liquid fuel, Angew. Chem. Int. Ed. 59 (2020) 15014–15020.

[40] C.J. Peng, G. Zeng, D.D. Ma, C. Cao, S. Zhou, X.T. Wu, Q.L. Zhu, Hydrangea-like superstructured micro/nanoreactor of topotactically converted ultrathin bismuth nanosheets for highly active CO_2 electroreduction to formate, ACS Appl. Mater. Interfaces 13 (2021) 20589–20597.

[41] S. He, F. Ni, Y. Ji, L. Wang, Y. Wen, H. Bai, G. Liu, Y. Zhang, Y. Li, B. Zhang, H. Peng, The p-orbital delocalization of main-group metals to boost CO_2 electroreduction, Angew. Chem. Int. Ed. 57 (2018) 16114–16119.

[42] H. Shin, Y. Ha, H. Kim, 2D covalent metals: a new materials domain of electrochemical CO_2 conversion with broken scaling relationship, J. Phys. Chem. Lett. 7 (2016) 4124–4129.

[43] J.K.N.B. Hammer, Why gold is the noblest of all the metals, Nature 376 (1995) 238–240.

[44] S. Li, P. Miao, Y. Zhang, J. Wu, B. Zhang, Y. Du, X. Han, J. Sun, P. Xu, Recent advances in plasmonic nanostructures for enhanced photocatalysis and electrocatalysis, Adv. Mater. 33 (2021), 2000086.

[45] X. Fu, J. Zhang, Y. Kang, Electrochemical reduction of CO_2 towards multi-carbon products via a two-step process, React. Chem. Eng. 6 (2021) 612–628.

[46] Z.W. Seh, J. Kibsgaard, C.F. Dickens, I. Chorkendorff, J.K. Norskov, T.F. Jaramillo, Combining theory and experiment in electrocatalysis: Insights into materials design, Science 355 (2017) B517.

[47] D. Voiry, H.S. Shin, K.P. Loh, M. Chhowalla, Low-dimensional catalysts for hydrogen evolution and CO_2 reduction, Nat. Rev. Chem. 2 (2018) 0105.

[48] P. Prabhu, V. Jose, J.-M. Lee, Heterostructured catalysts for electrocatalytic and photocatalytic carbon dioxide reduction, Adv. Funct. Mater. 30 (2020), 1910768.

[49] J. Wu, Y. Xie, Z. Ren, S. Du, H. Meng, L. Zhao, X. Wang, G. Wang, H. Fu, Porous palladium nanomeshes with enhanced electrochemical co2-into-syngas conversion over a wider applied potential, ChemSusChem 12 (2019) 3304–3311.

[50] J. Zhang, H. Li, P. Guo, H. Ma, X.S. Zhao, Rational design of graphitic carbon based nanostructures for advanced electrocatalysis, J. Mater. Chem. A 4 (2016) 8497–8511.

[51] Z.P. Jovanov, H.A. Hansen, A.S. Varela, P. Malacrida, A.A. Peterson, J.K. Nørskov, I.E.L. Stephens, I. Chorkendorff, Opportunities and challenges in the electrocatalysis of CO_2 and CO reduction using bifunctional surfaces: a theoretical and experimental study of Au–Cd alloys, J. Catal. 343 (2016) 215–231.

[52] F. Bienen, A. Löwe, J. Hildebrand, S. Hertle, D. Schonvogel, D. Kopljar, N. Wagner, E. Klemm, K.A. Friedrich, Degradation study on tin- and bismuth-based gas-diffusion electrodes during electrochemical CO_2 reduction in highly alkaline media, J. Energy Chem. 62 (2021) 367–376.

[53] W. Luo, W. Xie, M. Li, J. Zhang, A. Züttel, 3D hierarchical porous indium catalyst for highly efficient electroreduction of CO_2, J. Mater. Chem. A 7 (2019) 4505–4515.

[54] L. Ye, X. Chen, Y. Gao, X. Ding, J. Hou, S. Cao, Ultrathin two-dimensional metal–organic framework nanosheets for efficient electrochemical CO_2 reduction, J. Energy Chem. 57 (2021) 627–631.

[55] C. Cao, D.D. Ma, J. Jia, Q. Xu, X.T. Wu, Q.L. Zhu, Divergent paths, same goal: a pair-electrosynthesis tactic for cost-efficient and exclusive formate production by metal-organic-framework-derived 2D electrocatalysts, Adv. Mater. 33 (2021), 2008631.

[56] H. Zhong, Y. Qiu, T. Zhang, X. Li, H. Zhang, X. Chen, Bismuth nanodendrites as a high performance electrocatalyst for selective conversion of CO_2 to formate, J. Mater. Chem. A 4 (2016) 13746–13753.

[57] C. Chen, B. Zhang, J. Zhong, Z. Cheng, Selective electrochemical CO_2 reduction over highly porous gold films, J. Mater. Chem. A 5 (2017) 21955–21964.

[58] M. Fan, S. Garbarino, G.A. Botton, A.C. Tavares, D. Guay, Selective electroreduction of CO_2 to formate on 3D [100] Pb dendrites with nanometer-sized needle-like tips, J. Mater. Chem. A 5 (2017) 20747–20756.

[59] H. Yang, Y. Wu, G. Li, Q. Lin, Q. Hu, Q. Zhang, J. Liu, C. He, Scalable production of efficient single-atom copper decorated carbon membranes for CO_2 electroreduction to methanol, J. Am. Chem. Soc. 141 (2019) 12717–12723.

[60] W.B.L.M.L. Li, W.T. Song, C. Wang, Y.F. Yao, C.P. Wu, W.J. Luo, Z.G. Zou, Do Cu substrates participate in bi electrocatalytic CO_2 reduction? ChemNanoMat 7 (2021) 128–133.

[61] F. Zhang, C. Chen, S. Yan, J. Zhong, B. Zhang, Z. Cheng, Cu@Bi nanocone induced efficient reduction of CO_2 to formate with high current density, Appl. Catal. A: Gen. 598 (2020), 117545.

[62] W. Lv, J. Zhou, J. Bei, R. Zhang, L. Wang, Q. Xu, W. Wang, Electrodeposition of nano-sized bismuth on copper foil as electrocatalyst for reduction of CO_2 to formate, Appl. Surf. Sci. 393 (2017) 191–196.

[63] S.F.M.K. Shiro Kishihara, The effect of pH on Flux and rejection of coloring matters on ultrafiltration of caramel color, Nippon Shokuhin Kogyo Gakkaishi 27 (1980) 7–10.

[64] W.R. FETZER, Analysis of caramel color, Ind. Eng. Chem. 10 (1938) 349.

[65] H. Huang, X. Li, J. Wang, F. Dong, P.K. Chu, T. Zhang, Y. Zhang, Anionic group self-doping as a promising strategy: band-gap engineering and multi-functional applications of high-performance CO_3^{2-}-doped $Bi_2O_2CO_3$, ACS Catal. 5 (2015) 4094–4103.

[66] L. Hao, L. Kang, H. Huang, L. Ye, K. Han, S. Yang, H. Yu, M. Batmunkh, Y. Zhang, T. Ma, Surface-halogenation-induced atomic-site activation and local charge separation for superb CO_2 photoreduction, Adv. Mater. 31 (2019), 1900546.

[67] G. Wen, D.U. Lee, B. Ren, F.M. Hassan, G. Jiang, Z.P. Cano, J. Gostick, E. Croiset, Z. Bai, L. Yang, Z. Chen, Orbital interactions in Bi-Sn bimetallic electrocatalysts for

highly selective electrochemical CO_2 reduction toward formate production, Adv. Energy Mater. 8 (2018), 1802427.
[68] F. Yang, A.O. Elnabawy, R. Schimmenti, P. Song, J. Wang, Z. Peng, S. Yao, R. Deng, S. Song, Y. Lin, M. Mavrikakis, W. Xu, Bismuthene for highly efficient carbon dioxide electroreduction reaction, Nat. Commun. 11 (2020) 1088.
[69] Q. Lu, J. Rosen, Y. Zhou, G.S. Hutchings, Y.C. Kimmel, J.G. Chen, F. Jiao, A selective and efficient electrocatalyst for carbon dioxide reduction, Nat. Commun. 5 (2014) 3242.
[70] N. Han, Y. Wang, H. Yang, J. Deng, J. Wu, Y. Li, Y. Li, Ultrathin bismuth nanosheets from in situ topotactic transformation for selective electrocatalytic CO_2 reduction to formate, Nat. Commun. 9 (2018) 1320.
[71] S. Chen, Y. Su, P. Deng, R. Qi, J. Zhu, J. Chen, Z. Wang, L. Zhou, X. Guo, B.Y. Xia, Highly selective carbon dioxide electroreduction on structure-evolved copper perovskite oxide toward methane production, ACS Catal. 10 (2020) 4640–4646.
[72] W. Oh, C.K. Rhee, J.W. Han, B. Shong, Atomic and molecular adsorption on the Bi (111) surface: insights into catalytic CO_2 reduction, J. Phys. Chem. C 122 (2018) 23084–23090.
[73] M. Zhao, Y. Gu, W. Gao, P. Cui, H. Tang, X. Wei, H. Zhu, G. Li, S. Yan, X. Zhang, Z. Zou, Atom vacancies induced electron-rich surface of ultrathin Bi nanosheet for efficient electrochemical CO_2 reduction, Appl. Catal. B: Environ. 266 (2020), 118625.